ORIGINAL PAPER

Influence of Water Vapor and Local Gas Velocity on the Oxidation Kinetics of In625 at 900 °C: Experimental Study and CFD Gas Phase Simulation

Guillaume Duthoit[1] · Aurélie Vande Put[1] · Brigitte Caussat[2] · Hugues Vergnes[2] · Daniel Monceau[1]

Abstract

The effect of water vapor content on the oxidation behavior of In625 at 900 °C in synthetic air was reported. The higher the water vapor content, the greater the oxidation and volatilization rates were. Increasing the water vapor content led to an increase in the proportion of spinel and rutile-type oxides in the oxide scale compared to chromia, and the proportion of Al-rich oxides within the alloy. A k_p-k_v mass variation model was used to quantify the experimental results, and Fluent Ansys® CFD simulations of the gas phase were used to predict volatilization rates. CFD simulations were used to calculate local gas velocity, temperature and composition along with local volatilization rates at each point on the sample surface. It was possible to explain not only the variations in volatilization between upstream and downstream samples, but also the increased volatilization at sample corners. For longer durations, it was shown experimentally that the rate of volatilization decreases. This was explained by the enrichment of the oxide scale with spinel and rutile-type oxides.

Keywords Chromia-forming alloys · High-temperature oxidation · Water vapor · Gaseous environment · Volatilization · CFD simulation

Introduction

The development of H_2 combustion processes leads to a multiplication of high-temperature, water-rich oxidizing environments. However, adding water vapor accelerates volatilization and oxidation kinetics of chromia-forming alloys compared to oxidation in dry environment. Indeed, water vapor can react with chromia to produce Cr-rich volatile species [1] such as $CrO_2(OH)_2$ which is the predominant volatile specie to form above 600 °C in oxidizing and water-rich environments Eq. (1)

Extended author information available on the last page of the article

Springer

[2, 3]. The volatilization of chromia, alongside its growth, accelerates the Cr consumption and therefore shortens the life of the alloy [4–6]. Chromia growth follows a parabolic law while its volatilization into $CrO_2(OH)_2$ occurs at a constant rate [7, 8]. After a long enough duration and under humid condition, the oxide scale thickness becomes constant and the mass loss per unit area of the sample tends to a linear behavior with time which only depends on the volatilization rate [7, 8].

$$\frac{1}{2}Cr_2O_3 + \frac{3}{4}O_2 + H_2O = CrO_2(OH)_{2(g)} \tag{1}$$
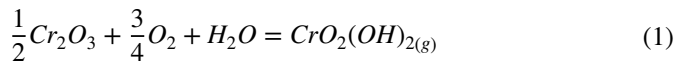
Several parameters influence the volatilization and oxidation kinetics as well as the oxide scale morphology and chemical composition. Water vapor content is known to increase volatilization kinetics [9]. Increasing gas velocity is known to increase the volatilization rate as it decreases the thickness of the boundary layer near the surface of the sample and therefore enhances the driving force for volatilization [10]. Also, the work of Oger et al. [11] on a chromia-forming austenitic alloy showed that at 900 °C under a humid atmosphere, samples exhibited different behaviors depending on their position in the test bench. By the use of computational fluid dynamic (CFD) simulation of the gas phase using Fluent Ansys®, the difference was associated with an enrichment in $CrO_2(OH)_2$ of the gaseous environment resulting from the volatilization reaction of the upstream sample Eq. (1), by such decreasing the driving force for volatilization of downstream samples. CFD simulation is a common tool to predict gas velocity and temperature profiles in the field of high-temperature oxidation [12–16]. Recently, CFD has been used by Jacobson et al. to estimate molar fractions of O_2 and SiO around a SiO_2 sample using the Hertz–Knudsen–Langmuir equation and the equilibrium vapor pressures [17]. In our group, we went further by calculating simultaneously the local molar fractions and volatilization rates that were assumed to be equal to the diffusive fluxes of volatile species leaving the sample surface. We thus simulated the gas phase of a rig containing three samples at a time, aligned in the gas flow direction [11]. Following the same methodology as the one of Oger et al., this study associated oxidation tests and gas phase simulation to understand the effect of inlet water vapor content and local gas velocity on the lifetime of Inconel 625 at 900 °C. However, the volatilization rate was not only different between samples but also on each sample as simulated by Jacobson et al. on a SiO_2 sample [17].

Experimental Procedures

The studied material is Inconel 625 (In625). Its chemical composition, measured by ignition spectroscopy, can be found in Table 1.

Three cylindrical samples of 12 mm in diameter and 1.5 mm in thickness were used for each experiment. They also featured a hole of 1.5 mm diameter pierced in the upper part of the sample and a chamfer of 0.5 mm on one of the sides of the samples to differentiate their front and their back, as shown in Fig. 1a. The samples were ground using SiC P600 paper and cleaned in ethanol under ultrasounds

**Table 1** Chemical composition of In625

	Ni	Cr	Mo	Nb	Fe	Si	Ti	Mn	Al	C	N	Co	Cu	O	S
at%	Bal	26.70	4.67	1.90	3.38	0.21	0.32	0.09	0.37	0.10	0.059	0.14	0.14	0.014	0.0018
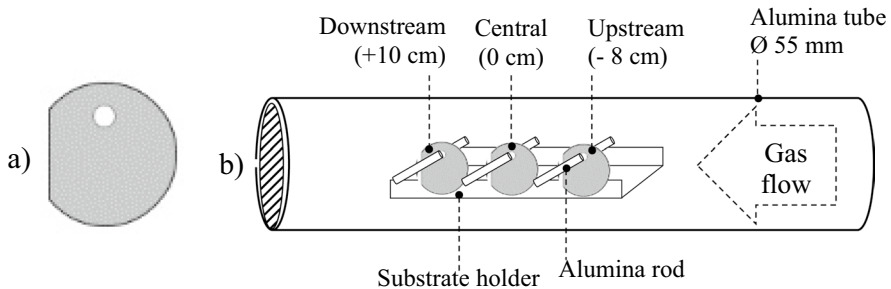
Fig. 1 **a** Sample scheme and **b** sample positioning within the furnace of the high-temperature oxidation rig

before testing. Then, they were oxidized at 900 °C under a gas flow of 220 or 250 sccm (0.62 or 0.7 cm/s at 900 °C) of a N_2-O_2-H_2O gas mixture with three different inlet water vapor contents: dry air, 12 vol. % and 30 vol. % The atmosphere was created by passing a mixture of synthetic N_2 and O_2 with air-like proportions through a bubbler containing distilled water to be then introduced into an oxidation rig of 55 mm diameter and a 20 cm long isothermal zone in which the samples were positioned (Fig. 1b). The isothermal zone was defined as the zone in which the rig walls and samples temperatures were at 900 °C $\pm$ 2.5 °C. The samples were oxidized during 400 h and they were regularly taken out of the rig to monitor their mass variation using a Sartorius Genius (ME215-P) microbalance, with an accuracy of 20 µg. Each recorded mass was the average of three weightings. At the end of the oxidation experiments, the samples surface was characterized using θ-θ and low-incidence X-ray diffraction (XRD). XRD analyses were conducted using a copper anti-cathode ($\lambda = 1.54056$ Å) thanks to a BRUKER RX D8 GIXRD with a low incidence of 5°, a Bragg angle between 20 and 120° or 20 and 80° and with a step of 0.04° or 0.02° for θ-θ and low-incidence analysis, respectively. The acquisition time per step was 2 s in both settings. Scanning electron microscopy (SEM) and energy-dispersive X-ray analysis (EDX) allowed for both surface and crosscut observation and composition analysis with a FEI Quanta450 microscope using the backscattered electron (BSE) mode and a Bruker Quantax captor, respectively. For the crosscut analysis, the section was prepared with various grades of SiC paper and finished with 1 µm diamond paste. The mass variation of a sample subjected to oxidation and volatilization follows the law in Eq. (2) [7]:

$$\frac{dm}{dt} = \frac{k_p}{2m_O} - k_v \qquad (2)$$

where m in $mg.cm^{-2}$ is the mass variation of the sample per unit area, k_p in $mg^2.cm^{-4}.s^{-1}$ and k_v in $mg.cm^{-2}.s^{-1}$ are, respectively, the oxidation and volatilization kinetic constants and m_O in $mg.cm^{-2}$ is the mass gain per unit area of oxygen in the oxide scale. A k_p-k_v model curve based on Eq. (2) was used to extract the oxidation and volatilization kinetic constants from experimental mass variation curves. The numerical model makes use of the ratio of oxygen mass over oxide mass in the oxide scale. This parameter was taken equal to the one of chromia. It was done by fitting as best as possible the net mass change curves resulting from the numerical integration of Eq. (2) (k_p-k_v model) to the experimental mass variation curves as presented in the next section (Fig. 2b).
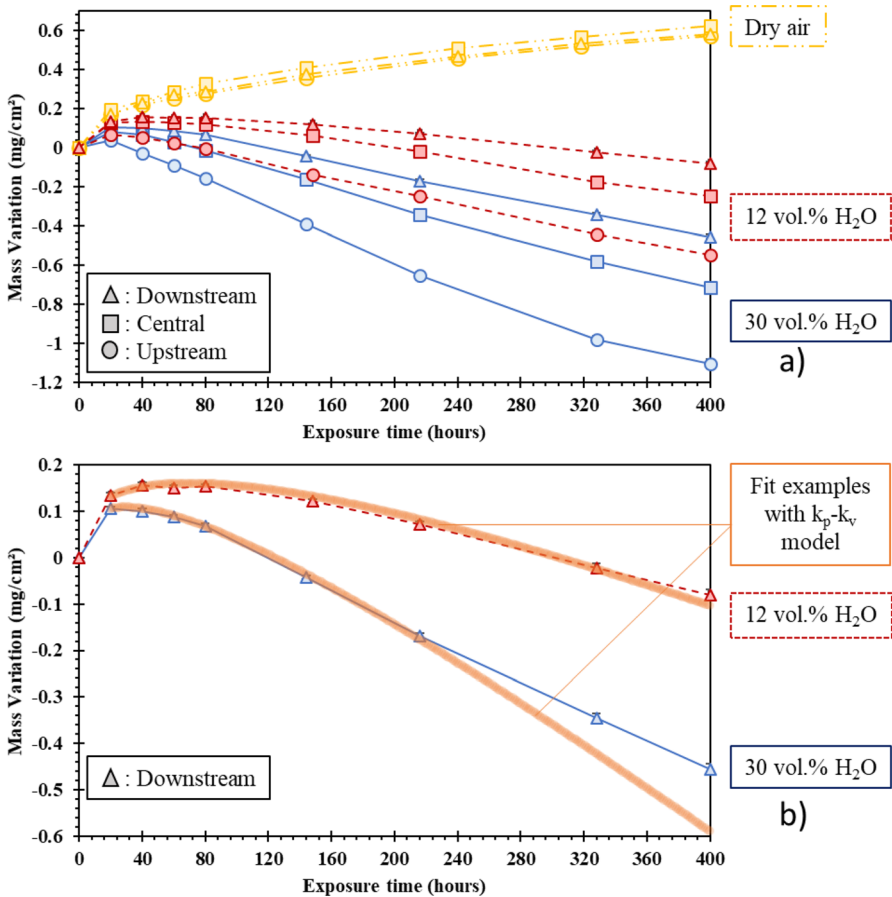
Fig. 2 **a** Mass variation of samples oxidized for 400 h at 900 °C under 3 different N_2-O_2-X%H_2O (vol. %) environments and **b** curves of the k_p-k_v model with the mass variation curves at 12 vol. % and 30 vol. % H_2O for downstream samples

The molar flux density of Cr_2O_3 volatilizing into $CrO_2(OH)_2$, $J_{CrO_2(OH)_2}$ in mol. $m^{-2}.s^{-1}$, was calculated by Fick's law Eq. (3) [18]:

$$J_{CrO_2(OH)_2} = \frac{D_{CrO_2(OH)_2}}{dRT} \times \left(P^s_{CrO_2(OH)_2} - P^\infty_{CrO_2(OH)_2} \right) \tag{3}$$

where $D_{CrO_2(OH)_2}$ in $m^2.s^{-1}$ represents the diffusion coefficient of $CrO_2(OH)_2$ in the gas phase and d in *m* stands for the characteristic length used in Fluent Ansys® to calculate diffusive fluxes. *R* is the ideal gas constant in $J.mol^{-1}$ K^{-1} and *T* is the temperature in K. $P^s_{CrO_2(OH)_2}$ in Pa is the partial pressure of $CrO_2(OH)_2$ at the surface of the sample and is assumed to be equal to the equilibrium partial pressure of $CrO_2(OH)_2$. $P^\infty_{CrO_2(OH)_2}$ in Pa is the partial pressure of $CrO_2(OH)_2$ in the free gas at the distance *d* from the surface. Regarding the gas phase simulation, Fluent Ansys® 2023 R1 was used to calculate local profiles of gas flow, temperature, molar fraction and volatilization rate. The same assumptions as the ones considered by Oger et al. [11] were applied in the present simulation work, i.e., steady-state conditions, laminar gas flow (consistent with Reynolds number < 1000), ideal gas, incompressible gas flow due to the low Mach number < 0.04 in the rig. As performed by Oger et al. [11], the physical properties of O_2, N_2 and H_2O were calculated from the FLUENT database using the kinetic theory of gases. For $CrO_2(OH)_2$, data to calculate the Lennard–Jones parameters were not available and thus, mean values close to that used by Young et al. [4] were considered (collision diameter σ (equal to 4.5 Å) and characteristic energy of interaction ε (with ε/k equal to 340, k being the Boltzmann's constant)).

The following boundaries conditions were imposed:

- A classical no-slip condition was applied for the gas velocity on the solid surfaces: walls, sample surfaces, sample holder and alumina rods.
- A user-defined function (UDF) was used to impose the temperature profile experimentally measured on all the walls. The temperature of the samples was set at 900 °C, and the wall temperature of the inlet and outlet pipes were equal to 60 °C as experimentally measured.
- The mass flow density of each species (except N_2) on the samples surface was calculated from Eq. (3), considering the stoichiometric coefficients of Eq. (1). On all other surfaces, which were in inert alumina, these mass flow densities were considered as zero.
- At the outlet of the simulated rig, a pressure outlet boundary condition was applied. The total pressure was fixed at the operating pressure, equal to atmospheric pressure (101,325 kPa).

The volatilization reaction implemented into Fluent as a surface reaction was quantified thanks to a second UDF. Only the phenomena represented by Eq. (1) was considered, assuming that the surface of the samples was rapidly fully covered by Cr_2O_3 and thus that the chromia scale formation was not rate-limiting. The literature lacks accuracy about the free energy of Gibbs used in the equilibrium partial pressure law of the volatile species [2]. In the present work, it was considered as being

equal to 104 kJ.mol^{-1}, close to the values considered by Opila et al. [2]. The chromia activity was fixed to 1.

Results and Discussion

To determine the influence of water vapor content on the oxidation behavior of In625, three experiments were carried out at 900 °C in the oxidation rig. The gas flow was set at 220 sccm (0.62 cm/s at 900 °C) with dry air and N_2-18.5%O_2-12%H_2O and set at 250 sccm (0.7 cm/s at 900 °C) for N_2-14.7%O_2-30%H_2O (vol. %). Under dry air, samples mass variation followed a parabolic law typical of the growth of a protective oxide such as chromia (Fig. 2a). No volatilization seemed to have occurred, as expected. Indeed, under such conditions, the partial pressure of CrO_3 is equal to 2.3×10^{-10} atm (based on $Cr_2O_3 + 3/4O_2 = CrO_3$ reaction with a free energy of Gibbs of 204 J/mol) while the partial pressure of $CrO_2(OH)_2$ is equal to 7.9×10^{-7} atm under an environment composed of 12 vol. % H_2O and 18.5 vol. % O_2 for example. Under humid atmosphere, samples mass variation followed a paralinear law characteristic of oxide growth coupled with volatilization (Fig. 2a). Under dry air, the mass variations of the three samples were very close. Conversely, when oxidized under humid atmosphere, the upstream sample experienced the highest mass loss while the further the sample was from the upstream sample, the lower the mass loss was (Fig. 2a). Even though the distance between the upstream and central samples was smaller (8 cm) than between the central and downstream samples (10 cm), the mass loss discrepancies between the upstream and central samples were more important than between the central and downstream samples. The higher the water vapor content, the more important the mass loss and the larger the mass loss gap were between the samples of a same experiment (Fig. 2a).

All the oxidation and volatilization kinetic constants found with the k_p-k_v model are presented in Table 2 for the water-rich environments. The oxidation and the volatilization rates of chromia increased when increasing the water vapor content, in accordance with the literature. The k_p-k_v model fitted very well the mass variations for short oxidation times. Nevertheless, a gap between experimental values and the k_p-k_v model appeared for long durations (see the k_p-k_v model curve for 12 vol. %

Table 2 Experimental k_p and k_v, obtained by a numerical fit of the mass variation data for In625 samples oxidized for 400 h at 900 °C under the three N_2-O_2-X%H_2O environments and average value of the k_v parameter on the surface of each sample obtained by CFD for atmospheres with water vapor (U = Upstream; C = Central; D = Downstream)
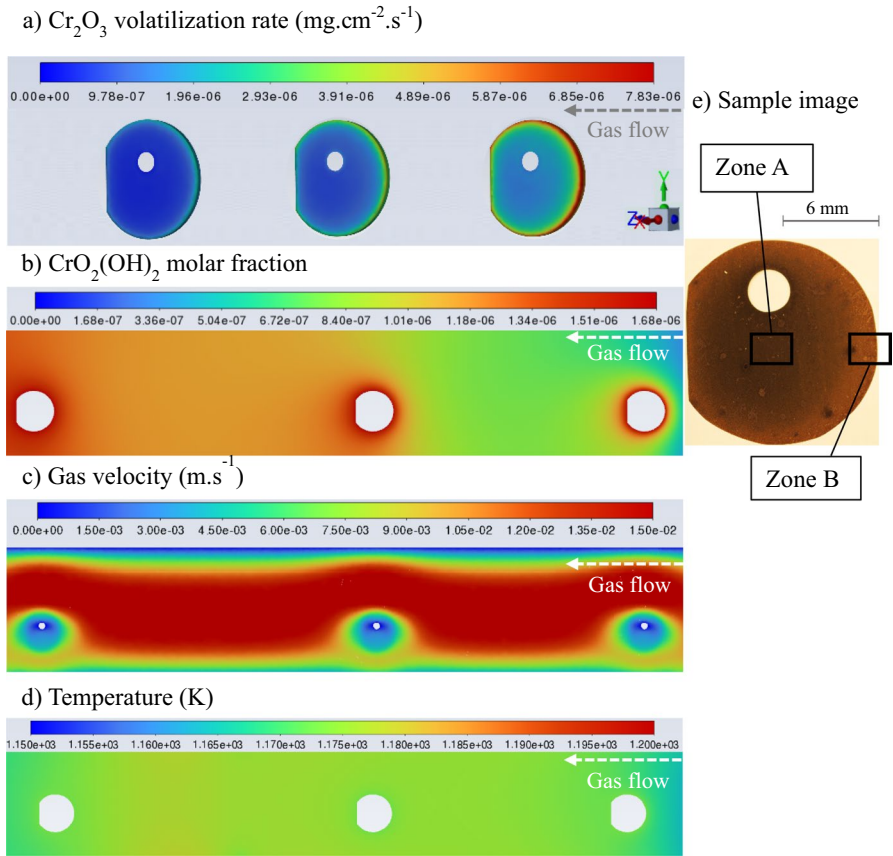
Atmosphere	Dry air			12 vol. % H_2O			30 vol. % H_2O		
Sample position	U	C	D	U	C	D	U	C	D
k_p (mg^2.cm^{-4}.s^{-1})$\times10^7$	2.2	2.7	2.4	3.5	3.5	3.5	4.0	4.0	4.0
k_v (mg.cm^{-2}.s^{-1})$\times10^7$	0	0	0	13	7.9	6.5	19	13	11
k_v based on CFD simulation (mg.cm^{-2}.s^{-1})$\times10^7$	N.A	N.A	N.A	14	7.3	4.0	36	20	12

H_2O in Fig. 2b). This clearly suggests a decrease in the experimental mass loss rate with time. For 12 vol. % H_2O, the k_p-k_v model managed to fit until around 320 h of oxidation while it fitted only until around 200 h for the experiment under 30 vol. % H_2O. The higher the water vapor content, the more the k_p-k_v model overestimated the mass loss of the sample at the end of the experiments. This is clearly due to a decrease in the experimental mass loss rate with time as already reported. Sand et al. observed a decrease in the volatilization rate with time for In690 samples oxidized in air + 20 vol. % H_2O at all temperatures and gas flows tested [19], as Stanislowski et al. who worked on stainless steels oxidized at 800 °C and 900 °C in air + 1.88 vol. % H_2O [20]. This could be due to a change in the oxide scale composition, leading to a decrease in Cr_2O_3 activity and therefore a reduced volatilization rate, whereas the model assumes a constant k_v. The volatilization rate values obtained using the k_p-k_v model correspond to an average of the volatilization rate over a sample. CFD simulation provided local k_v values that could be averaged over one sample (Table 2). Like for the k_p-k_v model, a better agreement between the experimental values and the CFD averaged ones was obtained at 12 vol. % H_2O than at 30 vol. % (Table 2). This is probably because the assumption made in the CFD simulations that the oxidized surface was composed of pure chromia is less satisfied at 30 vol. % H_2O, as detailed below.

In their work, Pineda-Arriaga et al. [1] oxidized samples of wrought In625 at 900 °C under dry synthetic air and found a k_p equal to 3.33×10^{-7} $mg^2.cm^{-4}.s^{-1}$ close to our values under dry air (Table 2). When it comes to k_v, the values presented on Table 2 are of the same order of magnitude than those of Sand et al. [19] or Stenzel et al. [21]. Sand et al. oxidized In690 at 800 °C, under a gas flow of 1000 sccm (250 sccm in our study) of air + 10 vol. % H_2O and found values of k_v between 6.25×10^{-7} $mg.cm^{-2}.s^{-1}$ and 8.3×10^{-7} $mg.cm^{-2}.s^{-1}$. On the other hand, Stenzel et al. worked with dense Cr_2O_3 oxidized at 850 and 950 °C under 0.1 cm/s of air + 10 vol. % H_2O and found values of k_v around 1.0×10^{-7} $mg.cm^{-2}.s^{-1}$ for 850 °C and around 1.5×10^{-7} $mg.cm^{-2}.s^{-1}$ at 950 °C. In our case, samples were oxidized either at different temperatures or for higher gas flows and higher water vapor contents, which could explain our greater values but the order of magnitude remains the same.

As observed by Oger et al. [11], the volatilization rate was the highest for the upstream sample and decreased progressively for the central and downstream samples (Table 2). In the samples zone, the experimentally measured sample surface and rig wall temperatures were of 900 ± 2.5 °C, as previously mentioned. Hence, the difference in k_v cannot be explained by a difference in temperature (as confirmed by the mass variation curves that are very close for the three samples under dry air).

However, the volatilization rate was not only different between samples but also on each sample. The CFD results under 30 vol. % H_2O indicate that it was higher on the edges and especially on the front edge of the samples and progressively decreased closer to the center of the samples (Fig. 3a). On the upstream sample simulated under 30 vol. % H_2O (where the highest discrepancies were calculated), volatilization rates would range between around 1×10^{-6} $mg.cm^{-2}$. s^{-1} on the center of the sample and almost 8×10^{-6} $mg.cm^{-2}.s^{-1}$ on the edges of the sample (Fig. 3a). This trend was due to the enrichment of the gas phase in

a) Cr_2O_3 volatilization rate (mg.cm^{-2}.s^{-1})


e) Sample image

b) $CrO_2(OH)_2$ molar fraction

c) Gas velocity (m.s^{-1})

d) Temperature (K)

Fig. 3 **a** Cr_2O_3 volatilization rate in mg.cm^{-2}.s^{-1}, **b** molar fraction of $CrO_2(OH)_2$ along the vertical YZ symmetry plane, **c** local gas velocity profile at a distance of 1 mm from the samples surface in m.s^{-1} simulated by CFD for samples oxidized under 250 sccm of N_2-14.7%O_2-30%H_2O (vol. %) at 900 °C, **d** local gas temperature profile in K along the vertical YZ symmetry plane and **e** picture of the upstream sample after 400 h of oxidation under the same conditions

$CrO_2(OH)_2$ (Fig. 3b) and also to the more important gas velocity near the sample edges than near their sides (Fig. 3c). As reported in the literature, the higher the local gas velocity, the higher the local volatilization rate [19]. It is also important to mention that the Reynolds number was close to 2 for the highest gas velocity calculated by CFD in the rig (2.5 cm/s). Therefore, the flow remained everywhere laminar. The gas temperature was close to 900 °C everywhere in the samples zone (Fig. 3d). In comparison with Fig. 3a, heterogeneity also appeared optically on all samples (as shown for one sample in Fig. 3e) on the same zones than in the simulations (The composition of these zones will be detailed below). The edges of the sample, more exposed to volatilization, appeared brighter than the rest of the sample, as reported in Sand et al. work on In690 [19].
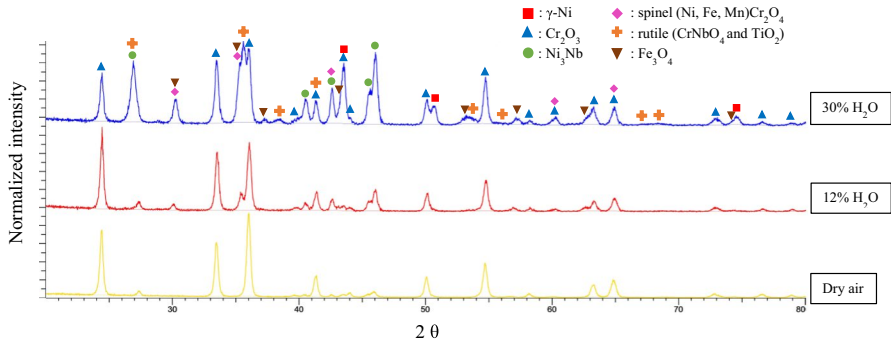
Fig. 4 Comparison of low-incidence (5°) XRD analysis in the center zone of upstream In625 samples oxidized for 400 h at 900 °C and under N_2-O_2-X%H_2O (vol. %)
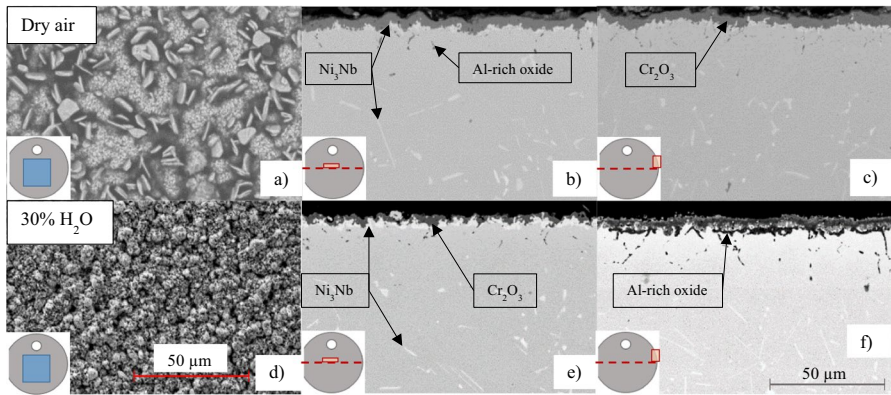
Fig. 5 **a**) SEM images of In625 upstream samples, exposed for 400 h at 900 °C under dry air on **a** the center zone of the surface, **b** the center zone of the crosscut section, **c** the front side of the crosscut section and exposed for 400 h at 900 °C under N_2-O_2-30%H_2O (vol. %) on **d** the center zone of the surface, **e** the center zone of the crosscut section, **f** the front side of the crosscut section

After the oxidation in dry air, low-incidence XRD analysis detected only one oxide structure: Cr_2O_3, in addition to δ-Ni_3Nb and γ-Ni phases which compose In625. When the oxidation was performed under humid conditions, two additional oxide structures were detected by XRD: spinel, rich in either Fe, Mn or Ni and rutile, either TiO_2 or $CrNbO_4$. The higher the water vapor content, the more intense the peaks for these oxides were, indicating an increase in their proportion in the oxide scale compared to chromia (Fig. 4).

Some observations of the samples surface were also made after oxidation by SEM, and some EDX analyses were done. They confirmed the XRD results and completed them. During the oxidation under dry air, equiaxe shaped and blade shaped chromia grains formed (Fig. 5a) while only equiaxe shaped oxide grains formed during the oxidations under humid conditions (Fig. 5d). Chromia grains

appeared denser under dry air than under humid conditions, as reported in Oger et al. work [11].

SEM–EDX showed that samples surface was covered by chromia for all conditions. However, on all samples surfaces Mn and Ti were always spotted at least as secondary elements, suggesting that their oxides formed even under dry conditions. To complete the simulation work that highlighted heterogeneous volatilization rates on the surface of each sample, observations of samples crosscut were made by SEM (Fig. 5b, c, e, f) and completed with EDX element cartographies (Fig. 6). Al-rich oxide precipitates (probably alumina) formed below the oxide scale for all conditions (Figs. 5b, c, e, f and 6). However, they were localized too deep below the surface to be detected by low-incidence XRD.

After oxidation under dry air, in crosscut sections no difference was noticed regarding the composition of the oxide scale between the center and the front side of the upstream sample. Chromia formed a dense oxide layer of 3.8 µm thick in the center zone (Fig. 5b) and 3.5 µm thick on the front side of the upstream sample (Fig. 5c). With the k_p value estimated with the k_p-k_v model, a value of 3.1 µm for the upstream and downstream samples and 3.7 µm for the central sample was expected after 400 h of oxidation which is consistent with experimental values. The oxide scale thickness did not changed much experimentally from one zone to another as no volatilization occurred. Under this oxide scale, a Ni_3Nb layer formed due to the effect of the Cr depletion on Nb activity (as explained by Chyrkin et al. [22]) as well as a few internal Al-rich oxides. Under humid conditions, the oxide scale differed depending on the location on the sample and the differences were exacerbated when increasing water vapor content. After 400 h of oxidation at 900 °C and under 30 vol. % water vapor, the chromia scale was thinner than under dry air in the center zone (Fig. 5e vs Fig. 5b) because of volatilization. In this area and this water-rich environment, the chromia scale was around 2.6 ± 0.3 µm thick. When considering that the volatilization in the center zone was of about 1.5×10^{-7} mg.cm^{-2}.s^{-1} (as visible in Fig. 3a) and with a k_p equal to 4×10^{-7} mg^2.cm^{-4}.s^{-1} (according to the k_p-k_v model based on (Eq. (2), Table 2), the k_p-k_v model anticipated an oxide scale 2.4 µm thick after 400 h of oxidation, which comes close to the experimental value. However, on the front edge of this sample, the chromia scale was around 3.6 ± 0.9 µm thick, based on image analysis. As explained previously, this was due to a higher gas velocity on
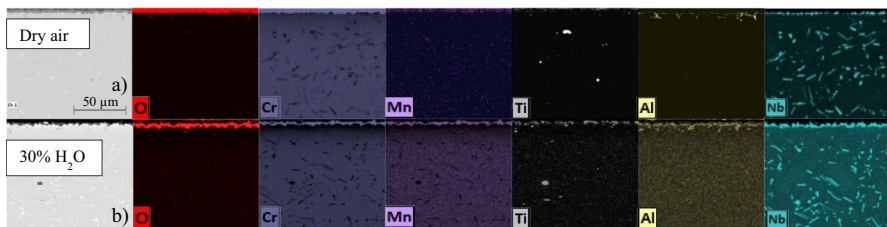
Fig. 6 SEM observation of crosscuts and EDX cartographies of the crosscut of In625 upstream samples in the center zone, exposed for 400 h at 900 °C under **a** dry air and **b** under N_2-O_2-30%H_2O (vol. %)

the front side compared to the center zone, leading to an increased volatilization and then to an important modification of the oxide scale nature and volatilization rate. Therefore, the k_p-k_v model could not anticipate the right oxide scale thickness as it cannot take into account the change in oxide scale composition. Also, under humid conditions, more Ni_3Nb accumulated under the oxide scale compared to dry air (Fig. 5e vs Fig. 5b), except on the front side of the upstream sample where no Ni_3Nb was visible (Fig. 5f). As reported in Huczkowski et al. work [23], this could be explained because (i) the Cr content reached a critical level at the oxide/alloy interface, leading to the oxidation of Ni_3Nb, and because (ii) the increase in oxygen activity due to the decrease in Cr activity allowed the formation of $CrNbO_4$ mixed oxide. On the front side again, Al-rich oxide almost formed a continuous scale (Fig. 5f) and was found deeper than on the center of the sample (Fig. 5e).

EDX element cartography (Fig. 6) gave complementary information that confirmed these modifications concerning the oxide scale composition. The enhanced brightness on element cartography for Fig. 6a makes it look like the oxide scale and is not visible on its whole but this is not the case, since, when looking at the SEM picture of Fig. 6a, the top of the oxide layer is visible. Under dry conditions on the center zone of the upstream sample, Mn, Ti, Al formed little precipitates within or below the oxide scale, while Nb almost formed a continuous scale at the oxide/alloy interface (Fig. 6a). On the other hand, under 30 vol. % of water vapor and on the center zone of the upstream sample, the Nb-rich layer was thicker than in dry air and the oxide scale appeared to be Mn-rich (Fig. 6b). Ti–rich oxides accumulated in the chromia scale and Al-rich oxides accumulated under it at 30 vol. % H_2O (Fig. 6b). Under humid conditions, the quantity of Ti and Mn oxides was not greater in absolute but relative to chromia. As the volatilization increased due to the increase in water vapor content, chromia was more consumed. Therefore, its relative content decreased and the relative amount of Mn and Ti oxides increased. However, for Ni, Nb and Fe oxides, their quantity did increase because of the large consumption of Cr in the alloy below the oxide scale, due to the larger volatilization of Cr_2O_3 under 30 vol. % of H_2O. The strong decrease in Cr content below the oxide scale in the areas where volatilization was the highest allowed Ni, Nb and Fe to oxidize. For Mn and Ti oxides, their presence was neither a consequence nor a cause, as they were always present and their absolute quantity did not change. However, the presence of Ni, Nb or Fe oxides was a direct consequence of chromia volatilization and more precisely of Cr depletion in the alloy, below the oxide scale.

Holcomb proposed that the growth of $MnCr_2O_4$ lessens the activity of Cr_2O_3 hence its volatilization rate [24]. Moreover, $MnCr_2O_4$ has a slower rate of volatilization than chromia [24] just like $CrNbO_4$ [23] which could mitigate mass loss. A greater proportion of TiO_2 within the oxide scale would also lower the volatilization rate compared to the CFD simulation which assumes a pure chromia scale. The significant proportion of $MnCr_2O_4$ and TiO_2 in the oxide scale when water vapor content was increased would explain why experimental values diverge with time from the k_p-k_v model under humid conditions and why CFD simulations overestimated volatilization rates.

Conclusion

In this work, water vapor appeared as a first order parameter regarding oxidation and volatilization behaviors of In625 oxide scale. As expected from the literature, increasing water vapor content enhanced oxidation and volatilization rates. Samples oxidized under humid conditions exhibited heterogeneous behaviors depending on their position in the experimental rig: upstream samples volatilized the most while downstream samples volatilized the least, as already observed by Oger et al. [11]. Samples also presented heterogeneities depending on the zone analyzed: the edges of samples volatilized the most while their center volatilized less. This last statement was explained by two reasons. The progressive enrichment in $CrO_2(OH)_2$ in the gas phase reduced the driving force of volatilization and areas exposed to lower gas velocities volatilized less. Under humid conditions, the chromia scale was thinner due to volatilization. The more a zone was exposed to volatilization, the more important the ratio of Mn and Ti oxide compared to chromia was in the oxide scale and the more Al-rich oxide grew below this oxide scale. It is then clear that in presence of water vapor, the oxidation scale cannot be anymore assumed to be composed of pure chromia, as it is the case in the present version of the CFD simulation. The changes in the oxide scale composition need to be considered in the gas phase simulation to better represent the volatilization rates. The approach we developed combining experiments, k_p-k_v model and CFD simulations allowed to better understand the cross-linked influence of the local gas velocity, local volatile species concentration and composition of the oxide scale on the oxidation and volatilization rates.

Author Contributions G.D wrote the main manuscript text, prepared all the figures and tables, conducted the experimental campaign and analyzed the results with the supervision of A.VP, B.C, D.M and H.V. A.VP conceived the experimental rig and designed the experimental route of the investigation. H.V wrote the UDF used to implement thermal profile and chemical reaction to the gas phase simulation. A.VP, B.C, D.M and H.V reviewed the manuscript.

Data Availability No datasets were generated or analyzed during the current study.

Declarations

Conflict of interest The authors declare that they have no known competing financial interests or personal relationships that could have appeared to influence the work reported in this paper.

References

1. K. Y. Pineda-Arriaga, J. Ramírez-Ramírez, F. A. Pérez-González, J. M. Alvarado-Orozco, R. Colás, and F. N. Garza-Montes-de-Oca, Oxidation in Water Vapor of Inconel 625 Fabricated by Additive Manufacturing. *High Temperature Corrosion of Materials*. **101**, 2024 (1–11).

2. E. J. Opila, D. L. Myers, N. S. Jacobson, I. M. B. Nielsen, D. F. Johnson, J. K. Olminsky, and M. D. Allendorf, Theoretical and Experimental Investigation of the Thermochemistry of $CrO_2(OH)_{2\,(g)}$. *The Journal of Physical Chemistry A*. **111**, (10), 2007 (1971–1980).

3. B. B. Ebbinghaus, Thermodynamics of Gas Phase Chromium Species: The Chromium Oxides, the Chromium Oxyhydroxides, and Volatility Calculations in Waste Incineration Processes. *Combustion and Flame*. **93**, (1–2), 1993 (119–137).

4. D. J. Young and B. A. Pint, Chromium Volatilization Rates from Cr_2O_3 Scales into Flowing Gases Containing Water Vapor. *Oxidation of Metals* **66**, (3–4), 2006 (137–53). https://doi.org/10.1007/s11085-006-9030-1.

5. S. R. J. Saunders, M. Monteiro, and F. Rizzo, The oxidation behaviour of metals and alloys at high temperatures in atmospheres containing water vapour: A review. *Progress in Material Science*. **53**, 2008 (775–837).

6. J. Shen, L. Zhou, and T. Li, High-temperature oxidation of Fe-Cr alloys in wet oxygen. *Oxidation of Metals*. **48**, 1997 (347).

7. Balbaud F, Desgranges C, Duhamel C, Marchetti L, Martinelli L, Molins R, Perrin S, Rouillard F. Corrosion et protection des matériaux à haute température. *Presse des Mines*. 2018

8. V. P. Deodeshmukh, Long-Term Performance of High-Temperature Foil Alloys in Water Vapor Containing Environment. Part II: Chromia Vaporization Behavior. *Oxidation of Metals* **79**, (5–6), 2013 (579–88). https://doi.org/10.1007/s11085-012-9344-0.

9. K. Zhang, A. El-Kharouf, T. Caykara, and R. Steinberger-Wilckens, Effect of Temperature and Water Content on the Oxidation Behaviour and Cr Evaporation of High-Cr Alloys for SOFC Cathode Air Preheaters. *High Temperature Corrosion of Materials*. **100**, (1–2), 2023 (21–45).

10. H. Asteman, J. E. Svensson, M. Norell, and L. G. Johansson, Influence of Water Vapor and Flow Rate on the High-Temperature Oxidation of 304L; Effect of Chromium Oxide Hydroxide Evaporation. *Oxidation of Metals*. **54**, (1–2), 1999 (2000).

11. L. Oger, H. Vergnes, B. Caussat, D. Monceau, and Put A. Vande, Fluid dynamic simulation of $CrO_2(OH)_2$ volatilization and gas phase evolution during the oxidation of a chromia forming alloy. *Corrosion Science*. **203**, 2023 110306.

12. M. Zancanaro, N. Bertrand, and F. Rebillat, Definition of Optimized Conditions to Extract Accurate Kinetic Laws from TGA Experiments: Modeling and Validation. *Oxidation of Metals*. **87**, (3–4), 2017 (393–402).

13. R. A. Golden and E. J. Opila, A Method for Assessing the Volatility of Oxides in High-Temperature High-Velocity Water Vapor. *Journal of the European Ceramic Society*. **36**, (5), 2016 (1135–47).

14. A. K. Sharma, W. Sagawa, Z. Ahmed, Y. Nishimura, and K. K. Okamoto, Integrated Experimental Assessment and Validation of Oxidation with Real-Scale SiC Fuel Compact in HTGR. *International Journal of Heat and Mass Transfer*. **220**, 2024 124930.

15. M. J. Ridley and E. J. Opila, Quantitative Evaluation of (0001) Sapphire Recession in High-Temperature High-Velocity Steamjet Exposures. *Journal of the European Ceramic Society*. **42**, (2), 2022 (631–37).

16. D. L. Myers, N. S. Jacobson, C. W. Bauschlicher, and E. J. Opila, Thermochemistry of Volatile Metal Hydroxides and Oxyhydroxides at Elevated Temperatures. *Journal of Materials Research*. **34**, (3), 2019 (394–407).

17. N. S. Jacobson, M. A. Kuczmarski, and B. A. Kowalski, Vaporization of Protective Oxide Films into Different Gas Atmospheres. *Oxidation of Metals.* **93**, 2020 (247–282).
18. W. Huang, T. Huang, P. Song, et al., $CrO_2(OH)_2$ volatilization rate and oxidation behavior prediction of the NiCr coating in air-H2O environment at 650 °C. *Corrosion Science.* **182**, 2021 109303.
19. T. Sand, C. Geers, Y. Cao, J. E. Svensson, and L. G. Johansson, Effective Reduction of Chromium-oxy-hydroxide Evaporation from Ni-Base Alloy 690. *Oxidation of Metals.* **92**, 2019 (259–279).
20. M. Stanislowski, E. Wessel, K. Hilpert, T. Markus, and L. Singheiser, Chromium Vaporization from High-Temperature Alloys. *Journal of The Electrochemical Society.* **154**, (4), 2007 (A295).
21. A. Stenzel, D. Fähsing, M. Schütze, and M. C. Galetz, Volatilization kinetics of chromium oxide, manganese oxide, and manganese chromium spinel at high temperatures in environments containing water vapor. *Materials and Corrosion.* **70**, (8), 2019 (1426–1438).
22. A. Chyrkin, P. Huczkowski, V. Shemet, et al., Sub-Scale Depletion and Enrichment Processes During High Temperature Oxidation of the Nickel Base Alloy 625 in the Temperature Range 900–1000 °C. *Oxidation of Metals.* **75**, 2011 (143–166).
23. P. Huczkowski, W. Lehnert, H. H. Angermann, A. Chyrkin, R. Pillai, D. Grüner, E. Hejrani, and W. J. Quadakkers, Effect of gas flow rate on oxidation behaviour of alloy 625 in wet air in the temperature range 900–1000 °C. *Materials and Corrosion.* **68**, (2), 2017 (159–170). https://doi.org/10.1002/maco.201608831.
24. G. R. Holcomb and D. E. Alman, The effect of manganese additions on the reactive evaporation of chromium in Ni–Cr alloys. *Scripta Materialia.* **54**, (10), 2006 (1821–1825).

Authors and Affiliations

Guillaume Duthoit[1] · Aurélie Vande Put[1] · Brigitte Caussat[2] · Hugues Vergnes[2] · Daniel Monceau[1]

✉ Guillaume Duthoit
guillaume.duthoit@toulouse-inp.fr

Aurélie Vande Put
aurelie.vandeput@toulouse-inp.fr

Brigitte Caussat
brigitte.caussat@toulouse-inp.fr

Hugues Vergnes
hugues.vergnes@toulouse-inp.fr

Daniel Monceau
daniel.monceau@toulouse-inp.fr

[1] CIRIMAT, Toulouse INP, Université Toulouse 3 Paul Sabatier, CNRS, Université de Toulouse, 4 allée Emile Monso, BP 44362, 31030 Toulouse Cedex 4, France

[2] LGC, INP-ENSIACET, CNRS, Université de Toulouse, 4 allée Emile Monso, CS 84234, 31432 Toulouse Cedex 4, France